

# The unsteady continuous adjoint method for minimizing flow-induced sound radiation

Christos Kapellos<sup>a,b,\*</sup>, Evangelos M. Papoutsis-Kiachagias<sup>a</sup>,  
Kyriakos C. Giannakoglou<sup>a</sup>, Michael Hartmann<sup>b</sup>

<sup>a</sup>*Parallel CFD & Optimization Unit, School of Mechanical Engineering, National Technical University of Athens, Heron Polytechniou 9, 15780 Zografou, Greece*

<sup>b</sup>*CAE Methods, Vehicle Technology, Volkswagen Group Research, Berliner Ring 2, 38436 Wolfsburg, Germany*

---

## Abstract

This paper develops the unsteady continuous adjoint method for aeroacoustic problems governed by time-dependent turbulent flows. To predict flow-induced sound radiation from a body in free-stream, an incompressible Improved Delayed Detached Eddy Simulation is firstly performed. The generated noise is then propagated with the Kirchhoff Integral method, which uses the pressure distribution on the body surface to compute the sound pressure at selected receivers. The continuous adjoint method for the aforementioned process is developed and presented for the first time. In the adjoint process, the differentiated Kirchhoff Integral is used to compute the boundary condition of the adjoint velocity on the body surface and, then, the unsteady adjoint equations are solved backwards in time. It should be noted that the time window where the simulation is performed and the time window over which the objective function is evaluated do not coincide. This is reflected on the adjoint boundary condition along the body and the time integration of the sensitivity derivatives. Furthermore, to ensure the consistency of the continuous adjoint-based gradients, grid sensitivities are taken into account. By incorporating the grid displacement equations during the mathematical development of the adjoint method, the surface integral of the residual of the flow PDEs, which is commonly omitted, is replaced with a

---

\*Corresponding author.

volume integral of the grid sensitivities and gives rise to the adjoint grid displacement equations along with an accurate sensitivity derivatives expression. The proposed method is verified against Finite Differences on a 3D turbulent flow around a cylinder and, then, applied to a real-world test case, concerned with the flow-induced sound radiation of the side mirror of the generic SAE vehicle.

*Keywords:* Continuous adjoint method, adjoint aeroacoustics, Kirchhoff Integral method, IDDES flow simulation, grid sensitivities, vehicle aeroacoustics

---

## 1. Introduction

The adjoint method has been established in engineering optimization workflows related to fluid mechanics, as it offers an efficient way to compute the gradient of objective functions, for use in gradient-based optimization. Both continuous [1, 2] and discrete [3, 4] adjoint formulations are in use in a wide range of applications for internal and external industrial flows [5, 6, 7, 8]. In the majority of these problems, the flows are governed or assumed to be governed by steady state equations. The main reason for this is that the unsteady adjoint method for real-world applications is extremely demanding in computational cost and storage requirements. With the advancements in computer technology, it has become possible to overcome these limitations and adjoint optimization for unsteady flows has started being used. This is imperative in scientific areas such as aeroacoustics where all problems are inherently unsteady. Nevertheless, recent works are still limited to mid-size test cases of low complexity flow problems [9, 10, 11]

This paper focuses on the formulation of the unsteady continuous adjoint method for real-world aeroacoustic problems governed by turbulent flows. The process presented here predicts the flow-induced sound field that is being radiated from an object in a free-stream. For low Mach number turbulent flows, it is safe to assume that the hydrodynamic pressure on the surface of the sound

radiating object dominates its acoustic counterpart [12]. Consequently, a flow solution provided by a high-fidelity unsteady incompressible flow solver is sufficient to resolve the physics of noise creation. The generated noise can be transmitted to the near- and far-field, either by solving additional equations, such as the Linearized Euler Equations, or with acoustic analogies, by computing volume or surface integrals which are analytical solutions of the Lighthill equation [13]. In this work, the Kirchhoff Integral method [14], which offers simplicity in implementation and accuracy for non-rotating configurations [15], is utilized. In order to obtain the sound pressure at a receiver, the pressure and its time and space derivatives, weighted by directivity coefficients, are integrated over a control surface surrounding the noise sources, namely the body in free-stream. The Ffowcs Williams-Hawkings (FW-H) equation [16] could be also used, however, for control surfaces on rigid bodies, this formulation leads essentially to the same sound sources on the body.

Once a process to compute the noise transmitted to the receiver from a body becomes available, the shape of the latter can be optimized through gradient-based optimization. The optimization target is to reduce the noise perceived by the receiver and the required gradient of the objective function with respect to (w.r.t.) the shape controlling parameters is computed with the adjoint method. The continuous adjoint formulation where the unsteady adjoint Navier-Stokes equations and the adjoint Kirchhoff Integral are derived, is presented in this paper. Following each shape modification within the optimization loop, grid displacement partial differential equations (PDEs) propagate the boundary displacement to the interior nodes, an action that should be taken into account during the continuous adjoint formulation. To do so, this paper extends the development presented in [17] for unsteady aeroacoustic problems. Adjoint grid displacement PDEs are derived and an additional term arises in the sensitivity derivatives expression. It is demonstrated that, in aeroacoustic gradient-based optimization, this formulation ensures the accuracy of the computed gradients with negligible computational burden.

The paper is structured as follows. Section 2 describes the governing equa-

tions for the flow-induced noise creation and propagation. An objective function suitable for aeroacoustics based on the time integral of squared acoustic pressure fluctuation computed at the receivers, is defined. The continuous adjoint formulation for the aeroacoustic problem is then described. Section 3 offers practical details about the implementation of the method, which is programmed in OpenFOAM<sup>®</sup>. In section 4, the proposed method is verified against finite differences, in the case of a turbulent flow around an isolated 3D cylinder. The accuracy of the proposed sensitivity derivatives expression is proven and the importance of taking grid sensitivities into consideration is convincingly demonstrated. In section 5, the method is applied to optimize the shape of the side mirror of a generic vehicle (SAE body) for the aforementioned objective function. Firstly, a sensitivity map analysis is conducted to investigate the influence the sensitivity derivative integration time window has on its computation but, also, to prove the importance of including the adjoint grid displacement equations. Finally, an optimization of the side mirror is performed, targeting at minimizing the radiated flow-induced sound at the vehicle’s side window, which is associated to the cabin noise level [18].

## **2. The continuous adjoint method for aeroacoustic problems**

This section presents the development of the continuous adjoint method, tailored for shape optimization problems in aeroacoustics. Firstly, the physical mechanisms of flow-induced noise creation and radiation are described and, then, the objective function, the corresponding adjoint field equations, boundary conditions and sensitivity derivatives expression are derived. Among the original contributions of this work are the differentiation of the acoustic analogy and the inclusion of the adjoint to the grid displacement model and the investigation of its effect on the accuracy of the computed gradients.

### *2.1. Prediction of flow-induced noise at a receiver*

In the presented method, the prediction of flow-induced noise at the receiver’s location from bodies in free stream is separated in two steps. The first step nu-

merically solves the flow around the body to compute the hydrodynamic pressure on its surface. In the second step, the acoustic propagation is carried out by means of the Kirchhoff Integral surface method.

The 3D unsteady Navier-Stokes equations, including a turbulence model, govern the incompressible fluid flow

$$R^p = \frac{\partial v_j}{\partial x_j} = 0 \quad (1)$$

$$R_i^v = \frac{\partial v_i}{\partial t} + v_j \frac{\partial v_i}{\partial x_j} - \frac{\partial \tau_{ij}}{\partial x_j} + \frac{\partial p}{\partial x_i} = 0, \quad i = 1, 2, 3 \quad (2)$$

where  $v_i$  are the velocity components,  $p$  the static pressure divided by the density,  $\tau_{ij} = (\nu + \nu_t) \left( \frac{\partial v_i}{\partial x_j} + \frac{\partial v_j}{\partial x_i} \right)$  the stress tensor and  $\nu$  and  $\nu_t$  are the bulk and turbulent viscosities, respectively. Throughout this paper, repeated indices in a term imply that the Einstein summation rule is applied.

The one-equation Spalart-Allmaras (S-A) turbulence model [19] is added to the primal equations and the Improved Delayed Detached Eddy Simulation (IDDES) technique [20] is used. This approach combines a Wall Modelled LES (WMLES) simulation, in the case with inflow turbulent content, and a DDES simulation otherwise. The subgrid length-scale of this strategy depends both on the grid spacings and the wall distance. Furthermore, by modifying the definition of the DDES length scale,  $l_{DDES}$ , the DDES behavior of the model gives an improved, compared to DES, RANS solution for attached regions and a DES-like for massively separated flows.

Upon convergence of the unsteady flow equations, the Kirchhoff Integral method is applied. This uses the pressure and its time and spatial derivative distribution on the selected Kirchhoff surface which, in this work, coincides with the body surface  $S_W$ , to compute the radiated acoustic field

$$p_{ac}(t, \vec{x}_{rec}) = \frac{1}{4\pi} \int_{S_W} \left[ -\frac{1}{R} \frac{\partial p}{\partial x_i} \hat{n}_i + \left( \frac{1}{R^2} p + \frac{1}{a_0 R} \frac{\partial p}{\partial t} \right) \hat{r}_i \hat{n}_i \right]_{ret} dS \quad (3)$$

at the receiver  $\vec{x}_{rec}$ . Here,  $a_0$  is the ambient speed of sound,  $\hat{n}$  the unit normal vector to  $S_W$  pointing towards the fluid,  $\vec{r} = \vec{x}_{rec} - \vec{x}$  the vector connecting the source and the receiver and  $R$  its magnitude whereas  $\hat{r} = \frac{\vec{r}}{R}$ . The r.h.s. of eq. 3

is expressed at the retarded time  $\tau = t - \frac{R}{a_0}$ , which is the time instant that a sound wave leaves the source to reach the receiver at  $t$ .

The terms on the r.h.s. of eq. 3 have a clear physical meaning; the first is known as thickness noise whereas the second and third as loading noise and are associated with the forces acting on it. In the flow problem, a zero Neumann condition is imposed on the pressure along  $S_W$ , so that the first term vanishes and the Kirchhoff integral reduces to

$$p_{ac}(t, \vec{x}_{rec}) = \frac{1}{4\pi} \int_{S_W} \underbrace{\left[ \frac{1}{R^2} p + \frac{1}{a_0 R} \frac{\partial p}{\partial t} \right]_{ret}}_{g_{ret,i}} \hat{r}_i \hat{n}_i dS \quad (4)$$

Hereafter,  $p_{ac}(t, \vec{x}_{rec})$  will be denoted by  $p_{ac}$ .

The noise perceived by the receiver is related to the fluctuation of the acoustic pressure  $p_{ac}$  computed by eq. 4. Consequently, a suitable objective function for shape optimization targeting minimal noise can be defined as the time-averaged squared acoustic pressure fluctuation

$$J = \frac{1}{T_{of}} \int_{T_{of}} (p_{ac} - \overline{p_{ac}})^2 dt = \frac{1}{T_{of}} \int_{T_{of}} p'_{ac}{}^2 dt \quad (5)$$

where the overbar denotes time-averaging over the time window  $T_{of}$ . In case a set of receivers is studied, the objective function is simply the sum of the r.h.s. integrals of eq. 5 over all receivers. For the sake of readability and without loss of generality, the mathematical development that follows considers only one receiver, even if the applications of section 5 include larger sets of receivers.

## 2.2. Grid displacement model

During the optimization process, the design variables  $b_n$ ,  $n = 1, \dots, N$  are updated and the body geometry is modified accordingly. The interior nodes of the computational grid must be displaced as well. The influence of the grid displacement must be taken into account for the gradient computation to be consistent in a numerical sense with the primal procedure. Any equation that propagates the boundary displacement into the interior grid nodes can be used

and, in this work, the Laplacian equations are chosen,

$$R_i^m = \frac{\partial^2 m_i}{\partial x_j^2} = 0, \quad i = 1, 2, 3 \quad (6)$$

where  $m_i$  are the Cartesian displacements of the grid nodes. Along  $S_w$ ,  $m_i$  are known from the current optimization step, while  $m_i = 0$  on the remaining boundaries,  $S \setminus S_w$ , which are not affected by the optimization.

### 2.3. Continuous adjoint formulation

Starting point of the continuous adjoint formulation is the definition of the augmented objective function  $L$  as the sum of  $J$  and the time and space integrals of the product of the primal residuals and the adjoint variable fields. The augmented objective function, thus, yields

$$L = J + \int_{T_s} \int_{\Omega} u_i R_i^v d\Omega dt + \int_{T_s} \int_{\Omega} q R^p d\Omega dt + \int_{\Omega} m_i^a R_i^m d\Omega \quad (7)$$

where  $T_s$  is the time window over which the primal equations, eqs. 1 and 2, are solved,  $u_i$ ,  $q$ ,  $m_i^a$  are the adjoint to the velocity  $v_i$ , pressure  $p$  and grid displacement  $m_i$ , respectively. Although an adjoint turbulence variable could have been introduced as in previous works from the authors' group [21], the frozen turbulence assumption is made in the applications presented in sections 4 and 5.

Time windows  $T_{of}$  and  $T_s$ , as defined in eqs. 5 and 7 respectively, do not necessarily coincide. In order to exclude transient phenomena occurring in the beginning of unsteady flow simulations, the flow equations are usually solved for a large time window  $T_s$ . After a sufficient interval of time, the integration of the objective function begins and is performed for a time window  $T_{of}$  being a part of time window  $T_s$ . This is why the general case in which  $T_s$  and  $T_{of}$  do not coincide is presented. Section 5 investigates further the selection of the two time windows by means of adjoint sensitivity maps on the side mirror of a generic vehicle.

The variation in  $L$  w.r.t.  $b_n$  is

$$\frac{\delta L}{\delta b_n} = \frac{\delta J}{\delta b_n} + \frac{\delta}{\delta b_n} \int_{T_s} \int_{\Omega} (u_i R_i^v + q R^p) d\Omega dt + \frac{\delta}{\delta b_n} \int_{\Omega} m_i^a R_i^m d\Omega \quad (8)$$

Each of the r.h.s. terms of eq. 8 is developed further as follows.

The total variation of any quantity  $\Phi$ , associated with position  $\vec{x}$  and retarded time  $\tau$ , w.r.t.  $b_n$ , is given by

$$\frac{\delta\Phi}{\delta b_n} = \underbrace{\frac{\partial\Phi}{\partial b_n}\Big|_{x,\tau}}_{T_1} + \underbrace{\frac{\partial\Phi}{\partial x_i}\Big|_{b,\tau} \frac{\delta x_i}{\delta b_n}}_{T_2} + \underbrace{\frac{\partial\Phi}{\partial\tau}\Big|_{b,x} \frac{\partial\tau}{\partial x_i}\Big|_b \frac{\delta x_i}{\delta b_n}}_{T_3} \quad (9)$$

where the subscripts on the right of each vertical bar are considered constant during differentiation. Terms  $T_1$  and  $T_2$  express the derivative of  $\Phi$  at a fixed retarded time  $\tau$ , as if any body shape change does not affect  $\tau$ , despite changes in distances.  $T_1$  denotes the derivative of  $\Phi$  by ignoring the effect of  $b_n$  on  $x_i$ , whereas  $T_2$  accounts for space changes at the same node (grid displacements, in the discrete sense) following changes in  $b_n$ , for a fixed field of  $\Phi$ . Term  $T_3$  indicates changes in  $\Phi$  because of a change in  $\tau$ , caused by a change in the relative position between the modified source point and the fixed receiver. Whenever  $\Phi$  is not expressed at the retarded time,  $T_3$  vanishes.

The differentiation of eq. 5 w.r.t.  $b_n$  yields

$$\frac{\delta J}{\delta b_n} = \frac{2}{T_{of}} \int_{T_{of}} p'_{ac} \left( \frac{\delta p_{ac}}{\delta b_n} - \frac{\delta \bar{p}_{ac}}{\delta b_n} \right) dt = \frac{2}{T_{of}} \int_{T_{of}} p'_{ac} \frac{\delta p_{ac}}{\delta b_n} dt \quad (10)$$

since  $\int_{T_{of}} p'_{ac} dt = 0$ .

The derivative of the acoustic pressure, eq. 4, is then expanded as

$$\frac{\delta p_{ac}}{\delta b_n} = \frac{1}{4\pi} \int_{S_w} \left[ \frac{\delta g_{ret,i}}{\delta b_n} \hat{n}_i dS + g_{ret,i} \frac{\delta(\hat{n}_i dS)}{\delta b_n} \right] \quad (11)$$

As the integrand of eq. 11 is expressed at the retarded time  $\tau$ , the derivative of  $g_{ret,i}$  is developed according to eq. 9 as

$$\begin{aligned} \frac{\delta}{\delta b_n} \left( \frac{\hat{r}_i}{R^2} p \right) &= \left[ \left( 3\hat{r}_i \hat{r}_j \frac{\delta x_j}{\delta b_n} - \frac{\delta x_i}{\delta b_n} \right) \frac{1}{R^3} \right] p \\ &+ \frac{\hat{r}_i}{R^2} \left[ \frac{\partial p}{\partial x_j} \frac{\delta x_j}{\delta b_n} + \frac{\partial p}{\partial t} \frac{\hat{r}_j}{a_0} \frac{\delta x_j}{\delta b_n} + \frac{\partial p}{\partial b_n} \right] \end{aligned} \quad (12)$$

and

$$\begin{aligned} \frac{\delta}{\delta b_n} \left( \frac{\hat{r}_i}{a_0 R} \frac{\partial p}{\partial t} \right) &= \left[ \left( 2\hat{r}_i \hat{r}_j \frac{\delta x_j}{\delta b_n} - \frac{\delta x_i}{\delta b_n} \right) \frac{1}{a_0 R^2} \right] \frac{\partial p}{\partial t} \\ &+ \frac{\hat{r}_i}{a_0 R} \left[ \frac{\partial^2 p}{\partial t \partial x_j} \frac{\delta x_j}{\delta b_n} + \frac{\partial^2 p}{\partial t^2} \frac{\hat{r}_j}{a_0} \frac{\delta x_j}{\delta b_n} + \frac{\partial^2 p}{\partial t \partial b_n} \right] \end{aligned} \quad (13)$$

where  $p$  and its derivatives are expressed at  $\tau$ .

By replacing eqs. 12 and 13 into 11, the derivative of the acoustic pressure radiated to a receiver from a source surface  $S_w$  w.r.t. the design variables  $b_n$  is given by

$$\begin{aligned}
\frac{\delta p_{ac}}{\delta b_n}(t, \vec{x}_{rec}) &= \frac{1}{4\pi} \int_{S_w} (3\hat{r}_i \hat{n}_i \hat{r}_j - \hat{n}_j) \left[ \frac{1}{R^3} p + \frac{1}{a_0 R^2} \frac{\partial p}{\partial t} \right]_{ret} \frac{\delta x_j}{\delta b_n} dS \\
&+ \frac{1}{4\pi} \int_{S_w} \left[ \frac{\hat{r}_i \hat{n}_i}{R^2} \frac{\partial p}{\partial x_j} + \frac{\hat{r}_i \hat{n}_i}{a_0 R} \left( \frac{\partial^2 p}{\partial t \partial x_j} + \frac{\hat{r}_j}{a_0} \frac{\partial^2 p}{\partial t^2} \right) \right]_{ret} \frac{\delta x_j}{\delta b_n} dS \\
&+ \frac{1}{4\pi} \int_{S_w} \left[ \frac{\hat{r}_i \hat{n}_i}{R^2} \frac{\partial p}{\partial b_n} + \frac{\hat{r}_i \hat{n}_i}{a_0 R} \frac{\partial}{\partial t} \left( \frac{\partial p}{\partial b_n} \right) \right]_{ret} dS \\
&+ \frac{1}{4\pi} \int_{S_w} g_{ret,i} \frac{\delta(\hat{n}_i dS)}{\delta b_n}
\end{aligned} \tag{14}$$

On the r.h.s. of eq. 14, the time-varying flow quantities  $p$ ,  $\partial p/\partial t$ ,  $\partial^2 p/\partial t^2$  as well as their partial derivatives w.r.t. the design variables are expressed at the retarded time  $\tau$  which depends on the distance between the receiver and the corresponding sender.

Using the Leibniz theorem for differentiating volume integrals with variable boundaries, the second term on the r.h.s. of eq. 8 yields

$$\begin{aligned}
\frac{\delta}{\delta b_n} \int_{T_s} \int_{\Omega} (u_i R_i^v + q R^p) d\Omega dt &= \int_{T_s} \int_{\Omega} \left( u_i \frac{\partial R_i^v}{\partial b_n} + q \frac{\partial R^p}{\partial b_n} \right) d\Omega dt \\
&+ \int_{T_s} \int_S (u_i R_i^v + q R^p) n_k \frac{\delta x_k}{\delta b_n} dt dS
\end{aligned} \tag{15}$$

The first term on the r.h.s. of eq. 15 can be expanded further by using the Green-Gauss theorem along with eq. 9. This paper does not contribute further to the development of the aforementioned term which is based on the technique presented in [6], so is omitted.

Emphasis is laid on the surface integral on the r.h.s. of eq. 15. This term is usually omitted, under the questionable assumption that the Navier-Stokes equations are satisfied along the boundary. In aerodynamic shape optimization problems, [17] showed that this omission may have a great impact on the accuracy of the gradient. Furthermore, computing the Navier-Stokes equations' residuals along the boundaries may not be an error-free process, since the computation of second-order spatial derivatives on the boundaries of unstructured

grids is prone to inaccuracies. For this reason, this term is developed further, [17], and transforms into a volume integral of grid sensitivities  $\frac{\delta x_k}{\delta b_n}$

$$\begin{aligned} & \int_{T_s} \int_{S_w} (u_i R_i^u + q R^p) n_k \frac{\delta x_k}{\delta b_n} dS dt \\ = & - \int_{T_s} \int_{\Omega} \frac{\partial}{\partial x_j} \left\{ -u_i v_j \frac{\partial v_i}{\partial x_k} - u_j \frac{\partial p}{\partial x_k} - \tau_{ij}^a \frac{\partial x_i}{\partial x_k} + u_i \frac{\partial \tau_{ij}}{\partial x_k} + q \frac{\partial v_j}{\partial x_k} \right\} \frac{\delta x_k}{\delta b_n} d\Omega dt \end{aligned} \quad (16)$$

which should be considered in order to derive the adjoint equations and sensitivity derivatives.

The last term on the r.h.s. of eq. 8 is also expanded as follows, [17],

$$\begin{aligned} \frac{\delta}{\delta b_n} \int_{\Omega} m_i^a R_i^m d\Omega &= \int_S m_i^a n_j \frac{\partial}{\partial x_j} \left( \frac{\delta x_i}{\delta b_n} \right) dS - \int_{S_w} \frac{\partial m_i^a}{\partial x_j} n_j \frac{\delta x_i}{\delta b_n} dS \\ &+ \int_S \frac{\partial^2 m_i^a}{\partial x_j^2} \frac{\delta x_i}{\delta b_n} d\Omega + \int_S m_i^a R_i^m n_k \frac{\delta x_k}{\delta b_n} dS \end{aligned} \quad (17)$$

The derived expressions of all terms, eqs. 11, 14, 15, 16 and 17, can now be replaced into eq. 8. Zeroing the coefficients of  $\partial v_i / \partial b_n$ ,  $\partial p / \partial b_n$  and  $\delta x_i / \delta b_n$  in the derived field integrals, gives rise to the unsteady adjoint Navier-Stokes equations

$$R^q = -\frac{\partial u_j}{\partial x_j} = 0 \quad (18)$$

$$R_i^u = -\frac{\partial u_i}{\partial t} + u_j \frac{\partial v_j}{\partial x_i} - \frac{\partial (v_j u_i)}{\partial x_j} + \frac{\partial q}{\partial x_i} - \frac{\partial \tau_{ij}^a}{\partial x_j} = 0, \quad i = 1, 2, 3 \quad (19)$$

where  $\tau_{ij}^a = (\nu + \nu_t) \left( \frac{\partial u_i}{\partial x_j} + \frac{\partial u_j}{\partial x_i} \right)$  is the adjoint stress tensor. Eqs. 18 and 19 must be solved along with the adjoint grid displacement equations

$$\begin{aligned} R_k^{m^a} &= \frac{\partial^2 m_k^a}{\partial x_j^2} + \int_{T_s} \frac{\partial}{\partial x_j} \left\{ u_i v_j \frac{\partial v_i}{\partial x_k} + u_j \frac{\partial p}{\partial x_k} + \tau_{ij}^a \frac{\partial v_i}{\partial x_k} - u_i \frac{\partial \tau_{ij}}{\partial x_k} - q \frac{\partial v_j}{\partial x_k} \right\} dt \\ &+ u_i \frac{\partial v_i}{\partial x_k} \Big|_{t_{start}} = 0, \quad k = 1, 2, 3 \end{aligned} \quad (20)$$

where  $m_k^a$  is the adjoint to the grid displacements.

The unsteady adjoint equations, 19 and 18, are solved backwards in time. This is imposed by the derived initial condition, during the development of

the differentiation of the temporal derivative of the Navier-Stokes equations.

Thanks to the permutation  $\frac{\partial}{\partial b_n} \left( \frac{\partial v_i}{\partial t} \right) = \frac{\partial}{\partial t} \left( \frac{\partial v_i}{\partial b_n} \right)$ , we get

$$\begin{aligned}
\int_{T_s} \int_{\Omega} u_i \frac{\partial}{\partial b_n} \left( \frac{\partial v_i}{\partial t} \right) d\Omega dt &= - \int_{T_s} \int_{\Omega} \frac{\partial u_i}{\partial t} \frac{\partial v_i}{\partial b_n} d\Omega + \int_{\Omega} u_i \frac{\partial v_i}{\partial b_n} d\Omega \Big|_{t_{start}}^{t_{end}} \\
&= - \int_{T_s} \int_{\Omega} \frac{\partial u_i}{\partial t} \frac{\partial v_i}{\partial b_n} d\Omega + \int_{\Omega} u_i \frac{\partial v_i}{\partial b_n} d\Omega \Big|_{t_{end}} \\
&\quad - \int_{\Omega} u_i \frac{\delta v_i}{\delta b_n} d\Omega \Big|_{t_{start}} + \int_{\Omega} u_i \frac{\partial v_i}{\partial x_j} \frac{\delta x_j}{\delta b_n} d\Omega \Big|_{t_{start}} \quad (21)
\end{aligned}$$

where  $t_{end} = t_{start} + T_s$ . The first term on the r.h.s. contributes to the field adjoint equations. A zero adjoint velocity condition is imposed at the end time of the primal computation to eliminate  $\partial v_i / \partial b_n \Big|_{t_{end}}$  appearing in the second term, resulting to the initial condition of the adjoint solution at the end. The third term is zero, since the flow velocity at  $t = t_{start}$  is independent of the design variables and the fourth one contributes as a source term to the adjoint grid displacement equations.

Similarly, by eliminating the coefficients of partial derivatives of the primal variables w.r.t.  $b_n$  in the surface integrals along the far-field and wall boundaries, the adjoint boundary conditions are derived. The boundary conditions  $m_i^a = 0$  is imposed along  $S$ , [17].

In addition to the development in [17], the primal and adjoint fields are time-dependent and, thus, the source term in the steady adjoint grid displacement equations, eqs. 20, includes one time integral over  $T_s$ . During the solution of eqs. 18 and 19, the computed primal/adjoint velocity and pressure fields are accumulated in time to obtain the source term of eqs. 20. Then, eqs. 20 can be solved as a post-processing step, once per optimization cycle, in order to compute the adjoint grid displacements  $m_i^a$ ,  $i = 1, 2, 3$ .

To derive the boundary condition of the  $u_i$  on the wall, the following integral, arising in the development of the first term on the r.h.s. of eq. 15, must be eliminated

$$\int_{T_s} \int_{S_w} \left( u_i + \frac{\partial J}{\partial p_{ac}} \frac{\partial p_{ac}}{\partial p} n_i \right) n_i \frac{\partial p}{\partial b_n} dS dt \quad (22)$$

The third integral on the r.h.s. of eq. 14 is replaced in eq. 22 and by setting the multiplier of  $\partial p/\partial b_n$  to zero, the wall adjoint velocity at time  $t$  yields

$$u_i = -\frac{1}{2\pi T_{of}} \left[ \frac{\hat{r}_j \hat{n}_j}{R^2} p'_{ac} - \frac{\hat{r}_j \hat{n}_j}{a_0 R} \frac{\partial p'_{ac}}{\partial t} \right]_{adv} n_i \quad (23)$$

The adjoint velocity has a constant direction that is normal to the surface and its instantaneous value at  $t$  depends on the acoustic pressure, computed at advance time  $\tau^{adv} = t + \frac{r}{c}$ . During the primal solution, the acoustic pressure and its temporal derivative at any receiver at time  $t$  are computed based on the contributions of the time instants at retarded time  $\tau$ . Conversely, the acoustic pressure and its time derivative contributing to the adjoint boundary condition at a time instant  $t$  are expressed at the ‘‘adjoint retarded’’ time, which is in fact an advanced time  $\tau^{adv}$ , given that the adjoint simulation runs backwards this time. Details about the algorithmic implementation can be found in section 3. Furthermore, since eq. 23 involves the differentiation of the objective function, it is valid only for the time window  $T_{of}$  and has no contribution, i.e.  $u_i = 0$ , at any other time instant of  $T_s$ .

After the derivation of the adjoint field equations and boundary conditions, the remaining terms of the mathematical development of eq. 8 yield the expression for the sensitivity derivatives along the wall boundary  $S_W$

$$\begin{aligned} \frac{\delta J}{\delta b_n} = & - \int_{T_s} \int_{S_W} \left( \tau_{ij}^a n_j - q n_i \right) \frac{\partial v_i}{\partial x_k} \frac{\delta x_k}{\delta b_n} dS dt \\ & - \int_{T_s} \int_{S_W} \left[ -u_k n_k \left( \tau_{ij} \frac{\delta(n_i n_j)}{\delta b_n} + \frac{\partial \tau_{ij}}{\partial x_k} \frac{\delta x_k}{\delta b_n} n_i n_j \right) \right] dS dt \\ & - \int_{S_W} \frac{\partial m_i^a}{\partial x_j} n_j \frac{\delta x_i}{\delta b_n} dS \\ & + \frac{1}{2\pi T_{of}} \int_{T_{of}} p'_{ac} \int_{S_W} (3\hat{r}_i \hat{n}_i \hat{r}_j - \hat{n}_j) \left[ \frac{1}{R^3} p + \frac{1}{a_0 R^2} \frac{\partial p}{\partial t} \right]_{ret} \frac{\delta x_j}{\delta b_n} dS dt \\ & + \frac{1}{2\pi T_{of}} \int_{T_{of}} p'_{ac} \int_{S_W} \left[ \frac{\hat{r}_i \hat{n}_i}{R^2} \frac{\partial p}{\partial x_j} + \frac{\hat{r}_i \hat{n}_i}{a_0 R} \left( \frac{\partial^2 p}{\partial t \partial x_j} + \frac{\hat{r}_j}{a_0} \frac{\partial^2 p}{\partial t^2} \right) \right]_{ret} \frac{\delta x_j}{\delta b_n} dS dt \\ & + \frac{1}{2\pi T_{of}} \int_{T_{of}} p'_{ac} \int_{S_W} g_{ret,i} \frac{\delta(\hat{n}_i dS)}{\delta b_n} dt \end{aligned} \quad (24)$$

The first two surface integrals indicate geometry changes which affect directly the flow and, consequently, the pressure distribution and noise creation on the

body. The third surface integral expresses the influence the change of the computational mesh has on the objective function; its significance in ensuring the accuracy of the sensitivities is demonstrated in the following section. Finally, the last three integrals are associated with the directivity of the sound field and how this is affected by geometry changes. It is important to point out the difference in the integration time windows of the sensitivity derivative terms; the first two are integrated over the simulation window  $T_s$  whereas the last three over the objective function window  $T_{of}$ .

### 3. Implementation and practicalities

The primal and adjoint flow simulations are performed in the OpenFOAM<sup>®</sup> environment. The flow equations are solved using the standard transient incompressible solver *pisoFoam*, utilizing a blending scheme for the convection term, which switches between a central second-order scheme at fine resolved areas and a second-order upwind scheme elsewhere, [22]. The adjoint equations are solved using an in-house adjoint OpenFOAM<sup>®</sup> solver, using the PISO algorithm, with a second outer iteration when needed, to converge the adjoint momentum equations more. For the convection term in the adjoint solution, a second-order downwind scheme is used. In the case of convergence instabilities that usually occur in industrial applications, a first-order scheme is used for the convection term and a dissipative limited scheme for the spatial gradient discretization of the so-called Adjoint Transpose Convection term,  $u_j \frac{\partial v_j}{\partial x_i}$ , in the adjoint momentum equation, eq. 19 .

As seen in eq. 19, the instantaneous primal velocities are needed for the backward time integration of the adjoint solution. Since storing all time steps requires a great amount of memory, the binomial checkpointing technique was used [23], where only a set of time steps, the so-called checkpoints, is stored.

The Kirchhoff Integral solver and its adjoint were programmed as a stand-alone library in the OpenFOAM<sup>®</sup> environment. During the primal solution (forward integration in time), the hydrodynamic pressure time-series on the

body is stored at each timestep. At the end, the Kirchhoff Integral, eq. 4, is computed, yielding the acoustic pressure at the receivers. A central eighth-order scheme with the equidistributed CFD time instants was used to compute all time derivatives. The acoustic pressure is computed and stored at the CFD timesteps. At each timestep, for every face of the Kirchhoff surface, the corresponding advanced time for each receiver is computed, which does not necessarily coincide with the CFD time-steps and (linear) interpolation is needed. To reduce the computation time and the computer memory requirements per processor, the implemented algorithm distributes variables computed at both senders and receivers to all processors in use, used for the flow solution. The last part of the algorithm computes the adjoint velocity boundary condition, eq. 23, and the three last integral terms of the sensitivity derivative expression, eq. 24. The adjoint velocity boundary conditions on the body surface are stored and called by the adjoint flow solver at each time step. The adjoint Kirchhoff Integral requires around twice as many computations as the primal one and thus has almost double computational cost.

#### 4. Verification of the computed sensitivity derivatives

In this section, the proposed method presented is verified against finite differences (FD) in a case concerning the unsteady turbulent flow around an isolated 3D cylinder. The Reynolds number based on the cylinder diameter  $D$  is  $Re_D = 500$ ; in this case, the wake exhibits fully turbulent behavior for a cylinder spanwise length greater than  $\pi$  diameters [24]. In this work, a spanwise length of 4 diameters was used for the cylinder and an O-Type grid consisting of 1.5 million cells was generated, with a far-field distance of  $15D$ . An initial run was performed for a total of 100s, in order to skip the transition phase. The computed flow fields at the end, fig. 1 were stored and used as initial conditions for the investigation that follows.

To modify the cylinder surface, the volumetric B-Splines morphing method, developed by NTUA [25], was utilized. A set of 8 control points was selected,

their x and y coordinates being the design variables  $b_n$  as shown in fig. 3. The derivatives of eq. 5 w.r.t.  $b_n$  were computed with central differences, where a step size equal to  $10^{-6}D$  was chosen, after conducting a study on independence of the step size. For each perturbation, the cylinder geometry was modified by the morpher and, afterwards, these displacements were propagated into the interior of the grid by solving eqs. 6.

The flow was then simulated for  $T_s = 10s$  and the objective function  $J$ , as in eq. 5, was computed for a time integral  $T_{of} = 10s = T_s$  at the receivers placed at a distance of  $15D$  on the z-plane crossing the middle of the cylinder, fig. 2.

The adjoint method developed in this work was used to obtain the sensitivities of  $J$  w.r.t.  $b_n$ . In fig. 3, the gradient values computed with FD are plotted against the ones computed with the adjoint method. To emphasize the importance of the sensitivity derivatives formulation presented in this paper, a second expression for the adjoint derivatives, commonly used in aerodynamic shape optimization, is presented for comparison. The latter, referred to as Surface Integral (SI) formulation in [17], makes the assumption that the surface integral over  $S_W$ , as shown in eq. 15, is zero. As it will be shown below, by neglecting this term, a significant error is introduced and the computed derivatives become inaccurate. Recall that the formulation presented in this paper, proposed as the Enhanced Surface Integral adjoint formulation (E-SI) in [17], substitutes this term by solving the adjoint grid displacement equations and enhancing the sensitivity derivatives expression with an additional surface integral,  $-\int_{S_W} \frac{\partial m_i^a}{\partial x_j} n_j \frac{\delta x_i}{\delta b_n} dS$ . The gradients computed with the proposed method are in a very good agreement with those computed with the FD scheme.

## 5. Application on the side mirror of the SAE body

In this case, the proposed adjoint-based optimization is applied to minimize the flow-induced sound radiation from the side mirror of a generic vehicle, the SAE body (fig. 4), to the vehicle's side window. Cabin noise is related to the acoustic load on the window, [26], so its minimization is a first step towards the

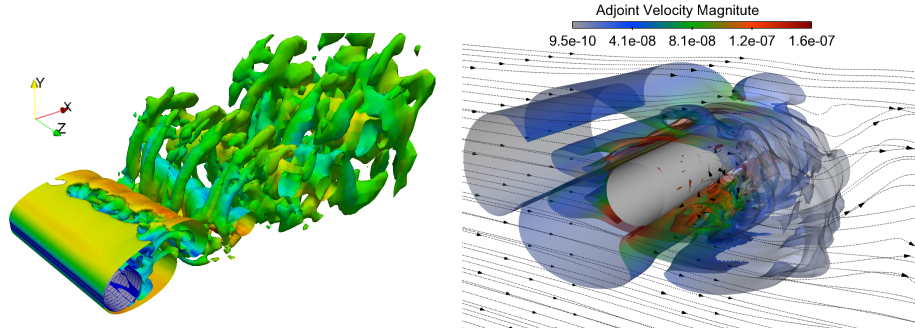


Figure 1: Turbulent flow around a 3D cylinder for  $Re=500$ . Left: Instantaneous flow structure visualized by the isosurface of  $Q = \frac{1}{8} (\|\nabla v - (\nabla v)^T\|^2 - \|\nabla v + (\nabla v)^T\|^2) = 10^{-1} s^{-2}$  and colored according to the velocity magnitude. Right: Adjoint vorticity iso-surfaces colored by the adjoint velocity magnitude ( $s^{-3}$ ). Black lines are the primal velocity streamlines.

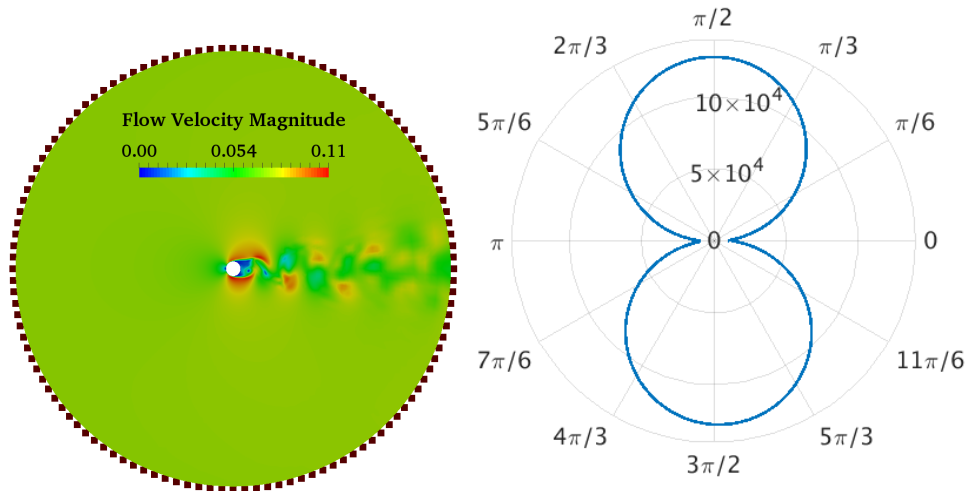


Figure 2: Turbulent flow around a 3D cylinder for  $Re=500$ . Instantaneous flow velocity at  $t = 10s$  on a  $z$ -Plane slice of the O-Type grid (left). Dark squares around the boundary represent the positions of the receivers, where the flow-induced sound radiation is assessed with the Kirchhoff Integral method. The directivity pattern (right) was computed for  $p_{ref} = 20 \mu Pa$ .

reduction of interior noise.

The computational grid, generated with the snappyHexMesh tool of OpenFOAM<sup>®</sup>, comprises 80 million cells, with a mesh resolution of 1mm on and around the mirror that resulted in 120000 faces-senders on the mirror surface. The receivers

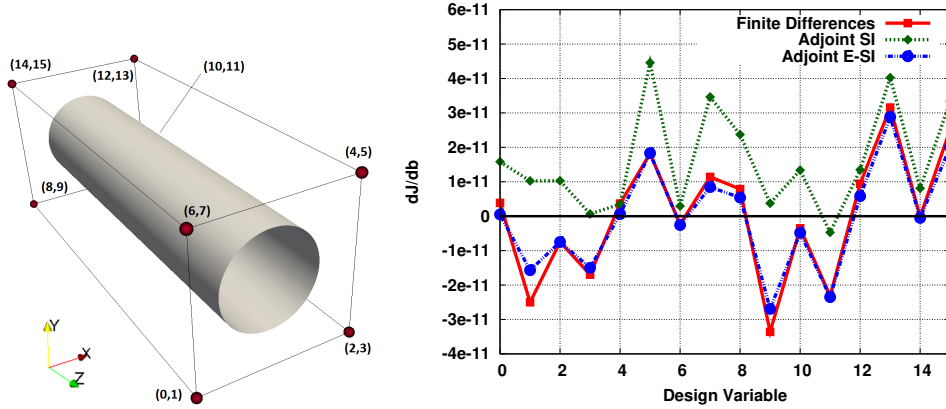


Figure 3: Turbulent flow around a 3D cylinder for  $Re=500$ . Left: Set of volumetric B-Splines control points used to parameterize the cylinder geometry. The degrees of freedom for each control point are the x and y coordinates, resulting in 16 design variables in total. Right: Comparison of the objective function gradient computed with FD and the adjoint method with and without considering the adjoint grid displacement. It is clear that the proposed adjoint gradient expression is crucial to ensure the accuracy of the method for aeroacoustic problems.

were distributed uniformly on the side window on a structured grid of 1 cm, not coinciding with the CFD surface grid nodes, leading to a total number of 10000. The A-pillar vortex and the mirror wake at a flow velocity of 40 m/s are shown in fig. 5(a). It is the interaction of these two typical vehicle flow structures that leads to strong pressure fluctuation on the mirror and, consequently, noise generation and radiation to all directions and to the vehicle side window, fig. 5(b).

### 5.1. Sensitivity map analysis

In what follows, flow-induced noise from the mirror is assessed with a flow computation for a total of 1.3s; the first 1s is used to skip the initial transient phase and during the last 0.3s, where the unsteady flow is considered to have reached a statistically stationary state, the acoustic pressure on the receivers and the objective function is computed. In order to compute consistent gradients, the adjoint flow must be simulated for the same primal time window of 1.3s. However, since only the last 0.3s affect directly the computation of the objective

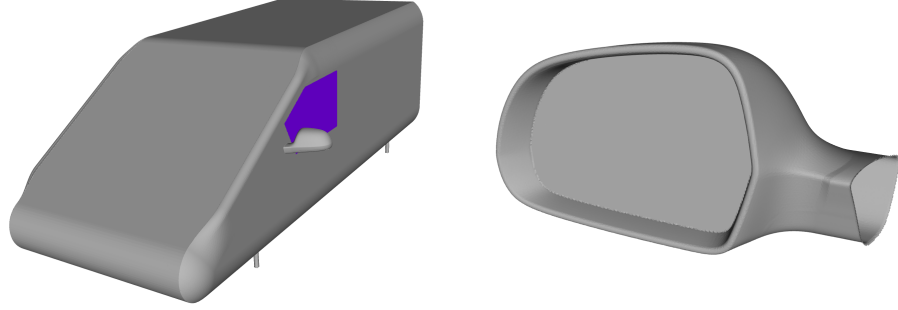


Figure 4: SAE Type 4 geometry: Front view of the SAE body (left). The area marked in purple is the vehicle’s side window, where 10000 receivers are placed and the radiated acoustic pressure is computed. A shape optimization of the side mirror (right) is performed, in order to reduce flow-induced noise radiation to the side window, which is quantified as the sum of eq. 5 over all receivers.

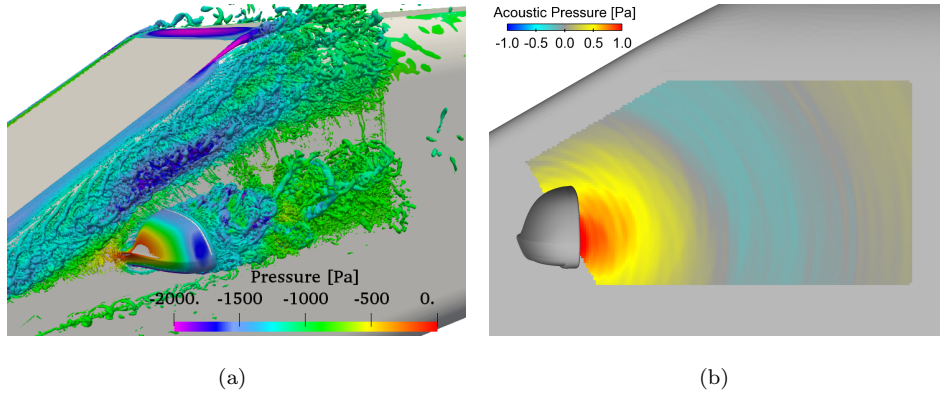


Figure 5: Turbulent flow around the SAE body: Instantaneous flow structure visualized by the isosurface of  $Q = \frac{1}{8} (\|\nabla v - (\nabla v)^T\|^2 - \|\nabla v + (\nabla v)^T\|^2) = 5 \cdot 10^5 s^{-2}$  and colored according to the velocity magnitude (left). Instantaneous acoustic pressure computed at the window with the Kirchhoff Integral method (right).

function, the question whether solving the adjoint equations over this shorter time window is equivalent, is intuitively raised. In the mathematical sense, this leads essentially to a different optimization problem, which focuses on the flow solution only on the last 0.3s, neglecting this way the initial transient phase. The study that follows sheds light on whether such an approach leads to a

correct outcome of the optimization procedure and can be used instead of the full adjoint simulation of 1.3s.

The two approaches examined are:

- *Approach A* computes the primal flow for a total of  $T_s = 1.3s$  and integrates the objective function for the last  $T_{of} = 0.3s$  of the simulation. The adjoint equations are then solved for the interval of  $T_s = 1.3s$  and the adjoint velocity boundary condition along the side mirror takes the eq. 23 only on the first  $T_{of} = 0.3s$  of the adjoint simulation and, afterwards, this is set to zero until the end of the simulation. The integral of eq. 20 and the first three terms of eq. 24 are integrated over  $T_s$ , while the last three terms of eq. 24 are integrated only over the first  $T_{of} = 0.3s$  of the adjoint solution (backwards in time), the time interval over which the objective function was evaluated during the primal simulation (forwards in time).
- *Approach B*, on the other hand, starts from the already converged unsteady flow field at  $t = 1s$ , computes the primal flow and evaluates the objective function for the remaining time, thus  $T_s = T_{of} = 0.3s$ . The adjoint solution and all terms of eq. 24 are integrated as well over the time integral  $T_s = 0.3s$ . This is consistent with the adjoint velocity boundary condition, eq. 23, as long as the initial field of each primal simulation during the optimization is kept the same and, thus, independent of the design variables, so that  $\delta v_i / \delta b_n |_{t_{start}} = 0$ .

The wall clock time for a single flow solution distributed at 960 CPUs was 90000s and 50000s for approaches A and B respectively, whereas for the Kirchhoff Integral computation, including its adjoint, 6000s. 60 checkpoints were used, requiring the equivalent of two primal flow recomputations per optimization cycle. Thus, the total computational cost for the sensitivity derivative computation was around 6 and 3 days, for approaches A and B respectively, without accounting for the additional overhead for mesh displacement and data management.

The computed sensitivity derivatives are presented on the side mirror of the SAE body, by means of the so-called sensitivity maps. They stand for the derivatives of the objective function w.r.t. the normal surface displacement, practically eq. 24 with  $\frac{\delta x_i}{\delta b_n} = n_i$ , and give an insight into the local geometry changes that may contribute to performance improvement. In fig. 6, areas that must be pulled outwards in order to reduce J, eq. 5, take blue colors whereas areas that must be pushed inwards are marked in red.

The two aeroacoustic sensitivity maps computed with approaches A and B are shown in fig. 6(a) and fig. 6(b) respectively. For both approaches, two main sensitive areas appear, the mirror neck and the casing of the mirror glass. In fig. 7, two cross sections over these two areas are presented. High sensitivities can be seen on the downwind edges of both the upper and lower side of the neck. As seen in fig. 7(b), flow separation occurs in this area, which creates pressure fluctuations that in turn generate and radiate noise. Similarly, on the edges around the casing of the mirror glass, the flow is disturbed by the geometry curvature or specific design features, such as the small step on the underside of the mirror, fig. 7(c). Although the sensitivities of both approaches focus on the same areas, differences arise on the way the mirror surface should be displaced. More distinctively, on the upper side of the mirror neck, approach A suggests an outward displacement on the part up to the downwind edge, where the sign changes and this area should be pushed inwards. On the contrary, approach B is dominated by an inward displacement on the upper side, with a small area of outward normal displacement in between.

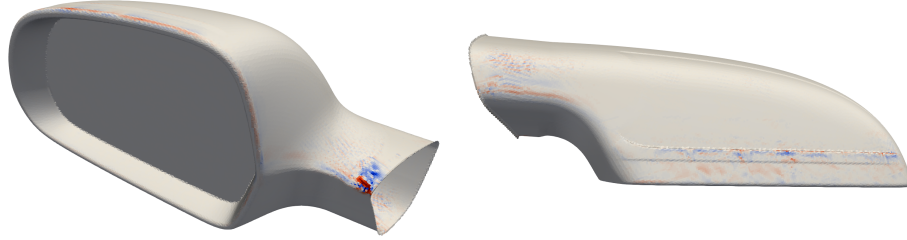
A morphing step was performed to show how this difference on the sensitivity maps translates to objective function change. The mirror was parameterized using the volumetric B-Splines method, similarly to section 4. 256 control points, 8, 4 and 8 in the x-, y- and z-direction, respectively, are used to define the part of the mirror geometry to be morphed. As seen in fig. 8, the control box surrounds the neck of the mirror which is the area with the highest potential in improvement. The placement of the bounding box is acceptable from the design point of view as well, as areas important for rain water management, such as

the mirror glass casing, are left intact. During the morphing, only the internal control points are allowed to vary and can move in all three directions, giving rise to 216 design variables in total. The maximum displacement of the control points led to an around  $1mm$  surface deformation.

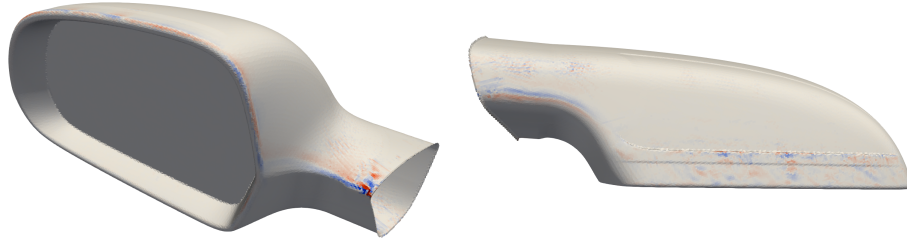
The morphed geometries are presented in fig.9 and the difference between the two approaches can be seen. The objective function for the two geometries was evaluated again. For approach A, the flow was recomputed from  $t = 0s$  and for  $T_s = 1.3s$ , and the objective function was integrated over the last  $0.3s$  of the simulation. Approach B used the previous primal flow initial condition at  $t = 1s$  and, then, the flow equations as well as the objective function were computed for  $T_s = T_{of} = 0.3s$ . The objective functions were reduced by 17% and 22% respectively, thus, each respective optimization problem is accurately solved. An additional run was performed for morphed mirror of approach B, using this time approach A, simulating a total of  $T_s = 1.3s$  and evaluating the objective function over the last  $T_{of} = 0.3s$ . The obtained value yielded a reduced objective function by 11% which, however, by taking into consideration the sensitivity map comparison, is rather coincidental.

Consequently, this study shows through the comparison of the sensitivity maps that, as expected based on the mathematical formulation, the adjoint gradients of approach B are not consistent with the primal evaluation process of approach A and may lead to a different solution. Whether this solution improves the objective function evaluated with approach A cannot be ensured and its use may be misleading for an optimization procedure.

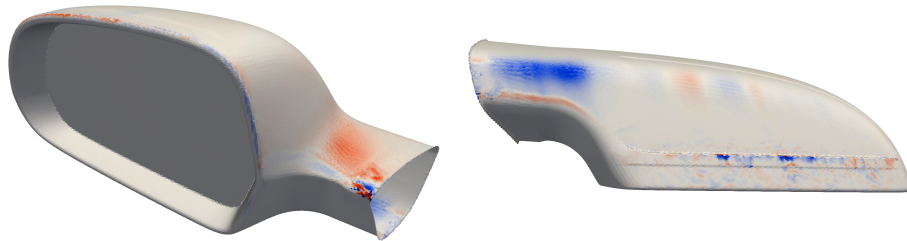
In addition, the significance of the proposed methodology that includes the grid displacement in its formulation can also be clearly visualized in fig.6(c). Similarly to section 4 and fig. 3, the sensitivity map computed based on the formulation without the surface integral  $-\int_{S_w} \frac{\partial m_i^a}{\partial x_j} n_j n_i dS$  in the sensitivity derivatives expression is presented. According to this map, an additional area on the top part of the mirror neck must be pushed inwards. These sensitivities guide in fact the optimization to the opposite direction, as the one that actually improved the objective function, as shown in the one-step displacement of fig.9(a).



(a) Approach A: the flow and adjoint equations were solved for  $T_s = 1.3s$ , and the objective function was evaluated for the time window of the last  $T_{of} = 0.3s$  of the simulation.



(b) Approach B: the flow and adjoint equations were solved from  $t = 1s$ , with the simulation and objective function time windows coinciding  $T_s = T_{of} = 0.3s$ .

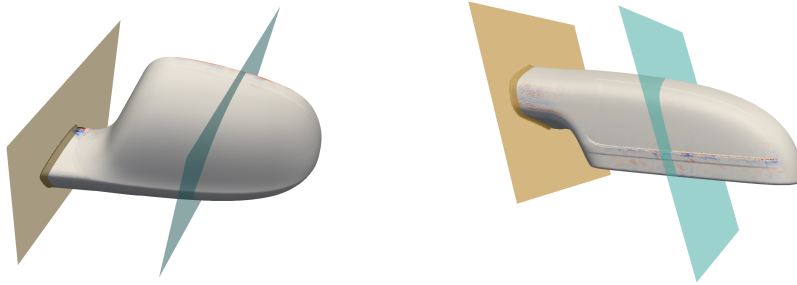


(c) Approach B: computed sensitivity map without taking into account the the adjoint grid displacement equation.

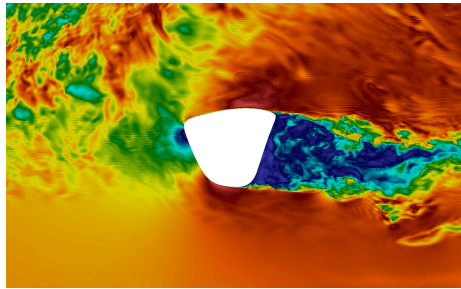
Figure 6: Flow-induced sound reduction on the SAE body: Adjoint sensitivity maps targeting at minimizing the radiated sound to the vehicle side window. Red areas must be pushed inwards whereas blue areas must be pulled outwards in order to minimize the objective function.

### 5.2. Optimizing the side mirror of the SAE body

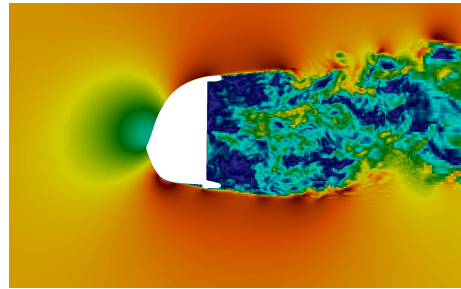
The side mirror of the SAE body, is optimized here, using approach A, as presented in subsection 5.1. Three optimization cycles were performed and the



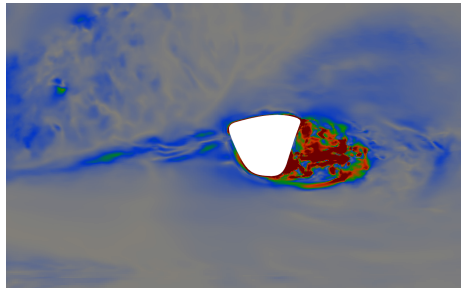
(a)



(b)



(c)



(d)

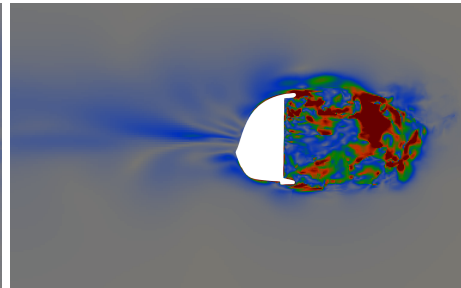


Figure 7: Flow-induced sound reduction on the SAE body: Two cross-sections over the mirror are presented. The first section covers the area around the mirror neck (depicted with the orange plane, first row), whereas the second the area around the casing of the mirror glass (depicted with the blue plane, first row). The primal (second row) and adjoint (third row) velocity magnitudes are shown for the mirror neck (left) and casing (right) cross-sections.

averaged squared acoustic pressure fluctuation computed at the side window, as defined in eq. 5, was reduced by 35%. The maximum displacement was around 2.6mm, and the total geometry displacement, projected on the normal

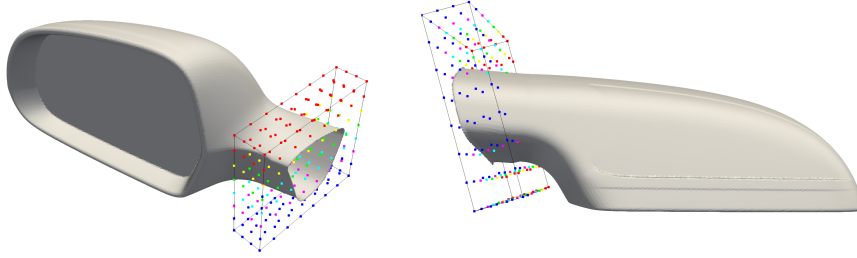
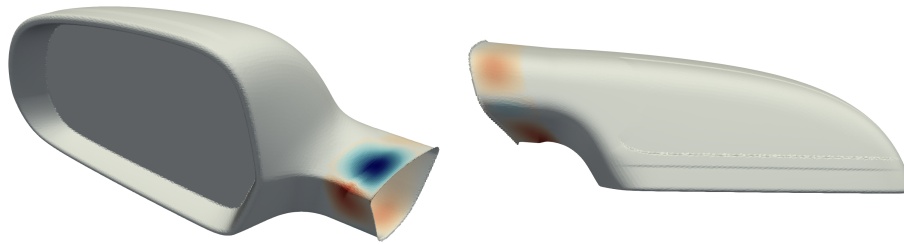
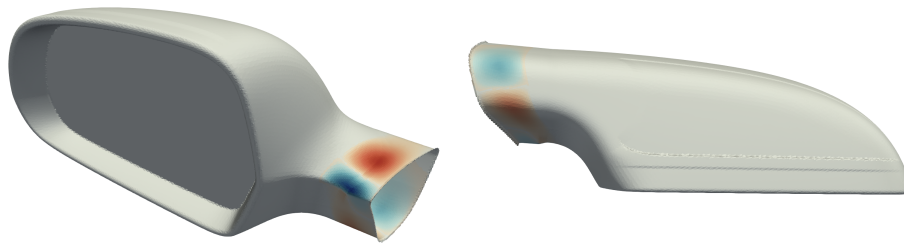


Figure 8: Flow-induced sound reduction on the SAE body: Bounding box of the control points of the volumetric B-Splines methods used to parameterize the mirror. The control points are coloured based on their  $z$ -coordinate, and during the optimization loop, only the internal points are allowed to vary.



(a) Approach A: the flow and adjoint equations were solved for  $T_s = 1.3s$ , and the objective function was evaluated for the time window of the last  $T_{of} = 0.3s$  of the simulation.



(b) Approach B: the flow and adjoint equations were solved from  $t = 1s$ , with the simulation and objective function time windows coinciding  $T_s = T_{of} = 0.3s$ .

Figure 9: Flow-induced sound reduction on the SAE body: Total normal displacement after one morphing step with the volumetric B-splines method. Red areas were pushed inwards, whereas blue areas were pulled outwards, in order to minimize the objective function.

direction is presented in fig. 10. Here, red areas were morphed inwards, while blue areas were morphed outwards. In fig. 11, the objective function  $J$  at each receiver placed on the side window is presented, as computed for the starting and optimized mirror geometry. The radiated sound has decreased in magnitude which is associated to the influence that the geometry change had to the flow and, thus, to sound generation. Moreover, by looking at the iso-lines of the squared acoustic pressure on the window, it is seen that the directivity of the generated sound field of the optimized mirror shape has moved upwind, affecting in this way less the area of the window.

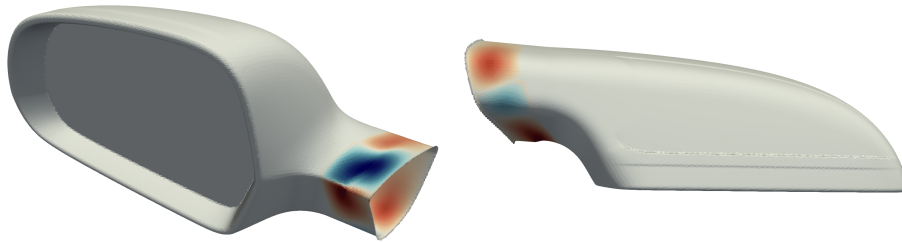


Figure 10: Flow-induced sound reduction on the SAE body: Total normal displacement performed during the optimization (top view left, bottom view right). Red areas indicate an inward to the surface displacement whereas blue areas an outward. With a maximum displacement of 2.6mm, the time-averaged squared acoustic pressure fluctuation radiated from the mirror to the side window was reduced by 35%.

## 6. Conclusions

The formulation of the continuous adjoint method for flow-induced sound radiation with the Kirchhoff Integral is presented in this paper for the first time in the literature. To predict the near- and far-field sound radiation from a body in free-stream, an incompressible IDDES simulation is performed, to resolve the noise creation phenomena, followed by the sound pressure propagation with the Kirchhoff Integral method, which uses the hydrodynamic pressure and its time derivative computed on the Kirchhoff surface, coinciding with the body's boundary.

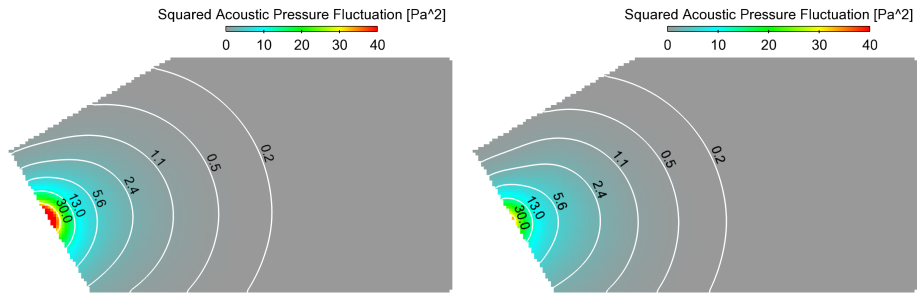


Figure 11: Flow-induced sound reduction on the SAE body: Time-averaged squared acoustic pressure fluctuation radiated to the side window from the starting (left) and the optimized (right) mirror. The optimization reduced the radiated sound magnitude and also pushed its directivity upwind, to have a smaller influence on the window.

To the authors knowledge, the unsteady continuous adjoint method has never been verified for unsteady turbulent flows or applied in problems of real-world complexity. In this paper, the efficiency and accuracy of the proposed methodology is demonstrated not only for a mid-size academic test case but also for a large-scale problem, the generic SAE body. In a 3D turbulent flow around a cylinder, a good agreement between the adjoint gradients computed by the proposed methodology and the FD gradients was achieved. It was shown that, in aeroacoustic shape optimization problems, it is important to incorporate grid displacement equations in the adjoint formulation, in order to account for grid sensitivities. Otherwise, the sensitivity derivative computation is prone to inaccuracies.

Furthermore, in the primal unsteady simulations, two time windows are commonly defined;  $T_s$ , where the flow equations are solved and  $T_{of}$ , placed at the end of  $T_s$ , where the objective function is evaluated. Their distinction was taken into account in the adjoint development and the derivation of the sensitivity derivative expression. A sensitivity map analysis was conducted for minimizing flow-induced noise radiation from the side mirror of the SAE body to its side window. It was demonstrated that, in order for the adjoint gradients

to be consistent with the primal problem, the adjoint equations must be solved over the exact time window  $T_s$ . In this case, the adjoint boundary conditions that depend on the objective function, here the adjoint velocity on the body, are active only over  $T_{of}$ . Solving the adjoint equations only for  $T_{of}$ , an approach that may seem intuitively reasonable, computes different gradient values which may be misleading during an optimization procedure. Based on these findings, 3 optimization cycles were performed and the obtained optimized shape of the mirror of the SAE body was displaced by a maximum of 2.6mm. The objective function, the time average of the squared sound pressure at the vehicle's side window, was minimized by 35%.

## 7. Acknowledgements

This work has been conducted within the "Industrial Optimal Design using Adjoint CFD" (IODA) project, funded by the European Union HORIZON 2020 Framework Programme for Research and Innovation under Grant Agreement No. 642959.

## References

- [1] A. Jameson, Aerodynamic design via control theory, *Journal of Scientific Computing* 3 (1988) 233–260.
- [2] W. Anderson, V. Venkatakrishnan, Aerodynamic design optimization on unstructured grids with a continuous adjoint formulation, *Computers & Fluids* 28 (1999) 443–480.
- [3] M. Giles, N. Pierce, Adjoint equations in CFD: duality, boundary conditions and solution behaviour, *AIAA Paper* 1997-1850.
- [4] M. Giles, N. Pierce, An introduction to the adjoint approach to design, *Flow, Turbulence and Combustion* 65 (2000) 393–415.
- [5] C. Othmer, Adjoint methods for car aerodynamics, *Journal of Mathematics in Industry* 4 (6) (2014) <https://doi.org/10.1186/2190-5983-4-6>.

- [6] E. Papoutsis, K. Giannakoglou, Continuous adjoint methods for turbulent flows, applied to shape and topology optimization: Industrial applications, *Archives of Computational Methods in Engineering* (2014) <http://dx.doi.org/10.1007/s11831-014-9141-9>.
- [7] N. K. Juern Krueger, T. Rung, Adjoint volume-of-fluid approaches for the hydrodynamic optimisation of ships, *Ship Technology Research* 65 (1) (2018) 47–68.
- [8] T. A. Tristan Dhert, J. R. Martins, Aerodynamic shape optimization of wind turbine blades using a Reynolds-Averaged Navier-Stokes model and an adjoint method, *Wind Energy* 20 (5) (2017) 909–926.
- [9] B. Zhou, T. Albring, N. Gauger, C. I. da Silva, T. Economon, J. Alonso, An efficient unsteady aerodynamic and aeroacoustic design framework using discrete adjoint, in: *17th AIAA/ISSMO Multidisciplinary Analysis and Optimization Conference*, Washington, D.C., 2016.
- [10] A. Carnarius, F. Thiele, E. Ozkaya, A. Nemili, N. Gauger, Optimal control of unsteady flows using a discrete and a continuous adjoint approach, *System Modeling and Optimization, IFIP Advances and Communication Technology* 391 (2013) 318–327.
- [11] S. R. K. Beckett Y. Zhou, Nicolas R. Gauger, W. Schroeder, A discrete adjoint approach for trailing-edge noise minimization using porous material, *Computational Methods in Applied Sciences* 36 (2015) 351–365.
- [12] J. Ask, L. Davidson, The sub-critical flow past a generic side mirror and its impact on sound generation and propagation, *AIAA Paper 2006-2558* <https://doi.org/10.2514/6.2006-2558>.
- [13] A. Lyrintzis, Surface integral methods in Computational Aeroacoustics - From the CFD near-field to the (acoustic) far-field, *International Journal of Aeroacoustics* 2 (2) (2003) 95–128.

- [14] H. A. K.R. Meadows, Towards a highly accurate implementation of the Kirchhoff approach for computational aeroacoustics, *Journal of Computational Acoustics* 4 (2) (1996) 225–241.
- [15] K. S. Brentner, F. Farassat, Modeling aerodynamically generated sound of helicopter rotors, *Progress in Aerospace Sciences* 39 (2-3) (2003) 83–120.
- [16] J. E. Ffowcs Williams, D. L. Hawkings, Sound generation by turbulence and surfaces in arbitrary motion, *Philosophical Transactions of the Royal Society of London* 264A (1969) 321–342.
- [17] I. Kavvadias, E. Papoutsis-Kiachagias, K. Giannakoglou, On the proper treatment of grid sensitivities in continuous adjoint methods for shape optimization, *Journal of Computational Physics* 301 (2015) 1–18.
- [18] A. Kabat vel Job, M. Hartmann, J. Sesterhenn, Prediction of the interior noise level for automotive applications based on time-domain methods, in: *INTER-NOISE 2016, Hamburg, 2016*.
- [19] P. Spalart, S. Allmaras, A one-equation turbulence model for aerodynamic flows, *AIAA Paper* 1992-0439.
- [20] M. Shur, P. Spalart, M. Strelets, A. Travin, A hybrid RANS-LES approach with delayed-DES and wall-modelled LES capabilities, *Journal of Heat and Fluid Flow* 29 (6) (2008) 1638–1649.
- [21] A. Zymaris, D. Papadimitriou, K. Giannakoglou, C. Othmer, Continuous adjoint approach to the Spalart-Allmaras turbulence model for incompressible flows, *Computers & Fluids* 38 (8) (2009) 1528–1538.
- [22] A. Travin, M. Shur, M. Strelets, P. Spalart, Physical and numerical upgrades in the detached-eddy simulation of complex turbulent flows, in: *412th Euromech Colloquium on LES and Complex Transitional and Turbulent Flows, Munich, Germany, 2012*.

- [23] Q. Wang, P. Moin, G. Iaccarino, Minimal repetition dynamic check-pointing algorithm for unsteady adjoint calculation, *SIAM Journal on Scientific Computing* 31 (4) (2009) 2549–2567.
- [24] G. Karniadakis, G. Triantafyllou, Three-dimensional dynamics and transition to turbulence in the wake of bluff objects, *Journal of Fluid Mechanics* 238 (1992) 1–30.
- [25] E. Papoutsis-Kiachagias, N. Magoulas, J. Mueller, C. Othmer, K. Giannakoglou, Noise reduction in car aerodynamics using a surrogate objective function and the continuous adjoint method with wall functions, *Computers and Fluids* 122 (2015) 223–232.
- [26] M. Hartmann, J. Ocker, T. Lemke, A. Mutzke, C. Schwarz, H. Tokuno, R. Toppinga, P. Unterlechner, G. Wickern, Wind noise caused by the a-pillar and the side mirror flow of a generic vehicle model, in: *AIAA Paper 2012-2205, 18th AIAA/CEAS Aeroacoustics Conference (33rd AIAA Aeroacoustics Conference)*, Colorado Springs, USA.